Diffusion in Inhomogeneous Media: Theory and Simulations Applied to Whole Cell Photobleach Recovery

Eric D. Siggia,* Jennifer Lippincott-Schwartz,† and Stefan Bekiranov*

*Center for Studies in Physics and Biology, The Rockefeller University, 1230 York Avenue, New York, NY 10021-6399; and †Cell Biology and Metabolism Branch, National Institute of Child Health and Human Development, Bethesda, MD 20892 USA

ABSTRACT A continuum description for diffusion in a simple model for an inhomogeneous but isotropic media is derived and implemented numerically. The locally averaged density of diffusible marker is input from experiment to define the sample. Then a single additional parameter, the effective diffusion constant, permits the quantitative simulation of diffusive relaxation from any initial condition. Using this simulation, it is possible to model the recovery of a fluorescently tagged protein in the endoplasmic reticulum (ER) after photobleaching a substantial region of a live cell, and fit an effective diffusion constant which is a property both of the geometry of the ER and the marker. Such quantitative measurements permit inferences about the topology and internal organization of this organelle.

INTRODUCTION

Photobleach measurements have been the method of choice for determining the diffusional mobility and the mobile fraction for fluorophores in solution or resident in a bilayer. Such studies have put on a quantitative basis the fluid mosaic model of the bilayer, and more recently pointed towards refinements of this model (Edidin, 1997). However, comparatively little is known about the physical properties of intracellular membrane compartments such as the endoplasmic reticulum (ER). The development of green fluorescent protein (GFP) has made it feasible to address such questions in living cells, (reviewed in Tsien, 1998; Ellenberg et al., 1999). Chimeric membrane proteins can be routinely constructed in which GFP is fused with a native cellular protein, which then localizes the chimera to the organelle of interest (reviewed in Lippincott-Schwartz et al., 1999; De Giorgi, 1999). The labeled cells appear normal, and many experiments have shown via colocalization with more conventional antibody markers in fixed cells that the localization is not altered by the GFP tag. The kinetics of protein trafficking from the ER to the Golgi complex (Presley et al., 1997; Scales et al., 1997), and then to the plasma membrane (Hirschberg et al., 1998; Polishchuk et al., 1999; Nakota et al., 1998; Toomre et al., 1999) have been followed in vivo this way, as well as the breakdown and reformation of such structures as the Golgi body (Zaal et al., 1999; Shima et al., 1998) and nuclear envelope (Ellenberg et al., 1997) during mitosis.

The ER is a geometrically complex compartment consisting of both tubular and cisternal components with complex and dynamic interconnections among them (Terasaki et al., 1986). Photobleaching technology has been used to characterize some of the fundamental physical properties of this organelle and its key molecular constituents. When is the ER a single connected membrane system (Terasaki et al., 1996; Ellenberg et al., 1997; Zaal et al., 1999; Subramanian and Meyer, 1997)? Are membrane and luminal proteins mobile (Szczesna-Skorupa et al., 1998; Marguet et al., 1999; Dayel et al., 1999; Nehls et al., 2000)? Do these properties change with drug treatments or during the cell cycle etc? However, the quantitative interpretation of such experiments is problematic, since in contrast to the plasma membrane, one cannot model the ER as an infinite flat sheet uniformly populated by fluorescent markers. One way to partially circumvent the geometric complexity of cellular organelles is to bleach as small a spot as possible in a region of the cell that looks homogeneous and interpret the recovery via previous formulas (Edidin, 1994; Peters et al., 1999). An alternative approach, which we analyze in this paper, is to bleach on the scale of the entire cell and in this way average over the small scale randomness that frequently is not optically resolved anyway (Sciaky et al., 1997; Ellenberg et al., 1997). An interesting and unexpected conclusion from a series of such studies on live cells is that diffusion viewed on the scale of microns matches to idealized physical theory better than for a diffraction-limited spot.

In this paper, we describe the circumstances under which diffusion in random media can be modeled by a continuum theory whose only free parameter is an effective diffusion constant, D_{eff}. Experiments can then be quantitatively fit to theory and D_{eff} becomes a useful characterization of the marker and the medium (e.g., organelle). With further assumptions, we relate D_{eff} to the microscopic diffusion constant measured for a homogeneous uniform media, e.g., an ideal flat bilayer in the case of a membrane protein. That diffusive recovery on a sufficiently large scale in the ER for instance, can be reduced to a general phenomenological equation should appear no more surprising than the ordinary diffusion equation, which makes no mention of the molecular processes that allow diffusion or atomic scale inhomogeneity in the substrate.

Received for publication 21 April 2000 and in final form 17 July 2000.

Corresponding author Dr. Eric Siggia, E-mail: siggia@eds1.rockefeller.edu.

0006-3495/00/10/1761/10 $2.00

Once one bleaches a fraction of the cell, the kinetics of the recovery will depend on the shape of the cell and where the remaining marker resides. The purpose of this paper is to develop the theory necessary to describe this process, implement it numerically, and illustrate how it can be used to fit an effective diffusion constant on a cell-by-cell basis. The physical recovery times required for this approach are longer than for spot photobleach because of the larger scales. Highly mobile markers can be accurately followed, and it is not even necessary to know the bleach region in advance or to bleach completely, because the recovery is followed beginning with the first postbleach image and is sensitive to the entire cell in one experiment. Using this approach, a single experiment can, in principle, determine whether a single diffusion constant applies throughout the cell.

THEORY

Two dimensions

We will phrase our derivation in the context of ER membranes in a cell viewed in projection with the photobleach, assumed to be uniform in the normal direction z. The limits of this idealization will be dealt with later.

Assume there is a passive membrane marker that does not interact with itself, is in equilibrium, and has the same microscopic diffusion constant in all parts of the ER; there is no immobile fraction. The marker density will appear nonuniform in a projected image; there will be a central void indicating the nucleus, a high concentration around it from the nuclear envelope and the greater thickness of cytoplasm in its vicinity; and then a gradual taper down to background levels at the boundary of the cell. The ER is a mixture of cisternae (sheets) and tubes with more total membrane around the nucleus than in the periphery. In theory, (though difficult to discern experimentally) the variable density, $\bar{\rho}(r)$, seen in projection could be due to a potential that concentrates the marker on certain sections of membrane, rather than there being simply more membrane in certain regions all marked with a uniform areal density. None of this significantly matters for what follows, provided the marker is not being actively pumped or concentrated; it must be in thermodynamic equilibrium. The process by which proteins are exported from the ER to the Golgi is clearly nonequilibrium.

Let $\vec{j}(r, t)$ denote the space- and time-dependent current of marker (units: mass/length-time in two dimensions) and $\rho(r, t)$ the analogous density. By definition of equilibrium, there will be no flux if ρ is a fixed (position-independent) multiple of $\bar{\rho}$. The current then must be:

$$j_i(r, t) = -\lambda_{i,j}(r)\nabla_j(\rho(r, t)/\bar{\rho}(r)) \tag{1}$$

If we average the densities over a region large enough for the connections within the network to appear isotropic, then it is plausible (as we justify further below) that the flux is proportional to $\bar{\rho}$, since all the material on the micro scale is equally mobile (i.e., $\bar{\rho}$ is equally well the density of conduits and we assume D_{eff} is position-independent)

$$\lambda_{i,j}(r) = D_{\text{eff}}\bar{\rho}(r)\delta_{i,j} \tag{2}$$

The central difficulty in treating diffusion in inhomogeneous media quantitatively is that number of channels for carrying material varies in space. To see how Eqs. 1 and 2 naturally incorporate this effect, consider a one-dimensional density $\bar{\rho}(x)$, as in Fig. 1, with an overall scale L and a constriction around $x = 0$ where $\bar{\rho} = \rho_0(1 + (x/\ell)^2)$, $\ell \ll L$, $\rho_0 \ll \bar{\rho}(\pm L/2)$. Assume a situation where for $x \ll 0$, $\rho(x)/\bar{\rho}(x) = r_-$ and $\rho = 0$ for $x \gg 0$. Then there is an approximate stationary solution ρ to the equation $j(r) = j_0$ with a constant flux, j_0, of material through the constriction given by

$$\rho/\bar{\rho} = r_- - j_0/(D_{\text{eff}}\rho_0)\int_{-\infty}^{x}(dx/(1 + (x/\ell)^2)) \tag{3}$$

and imposing the boundary condition at $x \gg 0$ yields

$$j_0 = D_{\text{eff}}r_-\rho_0/(\pi\ell) \tag{4}$$

Thus, the equilibration time between the right and left pools will be very long because of the constriction (and the relative density within the pools will have a small gradient in comparison with the restriction). Yet D_{eff} is the same everywhere.

The equation for the time dependence of ρ follows from (1–2) by conservation of material,

$$\partial\rho(r, t)/\partial t = D_{\text{eff}}\nabla\cdot(\bar{\rho}(r)\nabla(\rho(r, t)/\bar{\rho}(r))). \tag{5}$$

In the following, it will be useful to note the transformation that takes a solution ρ to Eq. 5 and generates another solution ρ',

$$\rho'(r, t) = cst_1\cdot\rho(r, t) + cst_2\cdot\bar{\rho}(r) \tag{6}$$

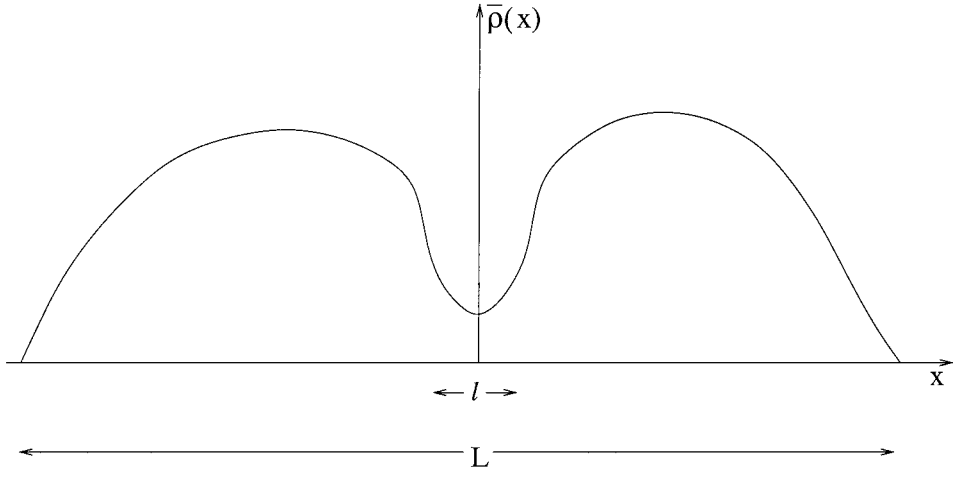

FIGURE 1 One dimensional density distribution $\bar{\rho}(x)$ representing two pools of proteins separated by a constriction of length l which was used to derive Eq. 4.

where $cst_{1,2}$ are numerical constants. When $\bar{\rho}$ is uniform, Eq. 5 reduces to the usual diffusion equation, and Eq. 6 reduces to the statement that a solution to the diffusion equation is invariant under rescaling or addition of an arbitrary constant. Near the boundary of the cell, where $\bar{\rho}$ tends to zero, the current vanishes and Eq. 5 conserves the integral of ρ over the cell. It can also be shown that for an image of area A

$$I = \frac{1}{A}\int d\mathbf{r}\bar{\rho}\left(\nabla\frac{\rho}{\bar{\rho}}\right)^2 \tag{7}$$

is monotone decreasing to 0 under Eq. 5, and its value is a useful averaged measure of the shortest scales present in the image.

It is instructive to rewrite Eq. 5 as

$$\partial\rho/\partial t + D_{\text{eff}}\nabla\cdot(p\nabla\ln(\bar{\rho}) - \nabla\rho) = 0 \tag{8}$$

This invites the interpretation of $\ln(\bar{\rho})$ as the negative of a potential $U(r)$ (temperature is one), in which case Eq. 8 becomes just the usual Fokker Planck equation for diffusive relaxation to the Boltzmann distribution in the presence of a one-body potential (Wang and Uhlenbeck, 1945). (Phrased in terms of $U(r)$, Fig. 1 should be inverted, and our calculation of the redistribution of material between the left and right pools is identical to the flux due to thermal activation over a potential barrier.) One can equally well attribute the spacial dependence of $\bar{\rho}$ to more membrane per projected area, $A(r)$, and thus write $\bar{\rho}(r) = A(r)e^{-U(r)}$. Hence our earlier remark that it is only $\bar{\rho}$ that matters in computing the relaxation, not $A(r)$ or $U(r)$; it is analogous to a free energy, with potentially both an entropic, A, and an enthalpic, U, contribution.

Real cells

The above formulas work in any number of dimensions, but with current instrumentation it is not feasible to follow in time photobleach recovery in three dimensions. Thus, it is necessary to consider the limitations inherent in two-dimensional images of a cell. The biggest problem is that two disjointed domains can appear connected in projection, and thus our model will impute a number of connections between them proportional to the projected density. For our model to be valid, we have to assume that the degree of interconnections is uniform across the cell; otherwise, D_{eff} would be a function of position. The same caveat applies to a network of tubules with restrictions (e.g., the model of Olveczky and Verkman, 1998). If there is a systematic variation in the number or severity of the restriction across the cell, then it can only be modeled as $D_{\text{eff}}(r)$.

For a three-dimensional slab of material described by Eq. 5, the density will become uniform in z, when it has diffused a horizontal distance of order the thickness. Thus errors of projection are minimized by photobleaching a portion of the cell much larger than its thickness. Nonuniformity of the bleach in z is also immaterial under the same circumstances.

An immobile fraction, provided it is a fixed numerical fraction γ_i of $\bar{\rho}(r)$, can be readily handled by the above formulas, since they can be applied to the mobile fraction only, by exploiting Eq. 6 to transform away the immobile part of $\bar{\rho}$ (n.b.: Eq. 5 is invariant under $\bar{\rho} \rightarrow (1 - \gamma_i)\bar{\rho}$). However, the initial conditions for the mobile fraction have to be computed from the experiment by determining the fraction of material $\gamma_p < 1$ bleached. So in the unbleached (respectively bleached) region, the prebleach mobile density is $(1 - \gamma_i)\bar{\rho}$ (respectively $1 - \gamma_i)\gamma_p\bar{\rho}$), which serves to initialize the numerical integration. The numerical solution as a function of time is then added to the immobile fraction (which is reduced by γ_p in the bleached region) to compare with experiment. We have not found a robust way to implement the most general situation, when the immobile fraction is a function of position, unrelated to $\bar{\rho}$, and mention potential problems in the discussion.

Two species with different D_{eff}, whose densities are both a fixed fraction of $\bar{\rho}$, can be handled by doing a single simulation, then adjusting an overall intensity and the time scale to match the concentration and diffusion rate for each component and adding the results.

Intuitively the microscopic diffusion constant (measured normal to a flat membrane) will be larger than D_{eff} to which it gives rise in a random geometry, since the marker is traveling farther than is measured in projection. To quantify this, imagine a network of tubes whose diameter is less than the scale on which they interconnect. After a short time to equalize the marker around the tubes, the diffusion will occur along a series of effectively one-dimensional segments. Let θ be the angle between a tube and the plane that is imaged. Then the current along the tube is larger by a factor $\cos(\theta)$ than its projection, whereas the marker gradient is smaller by the same factor in the two cases. Because the diffusion constant is the ratio of flux to gradient,

$$D_{\text{eff}} = \langle\cos^2(\theta)\rangle D_0 = D_0/d \tag{9}$$

where to average the angle it was assumed that the tubes are isotropically distributed in either $d = 2$ or $d = 3$ dimensions. The same relation holds for a luminal marker.

A similar relation can be derived when the marker is confined to a sheet in three dimensions with unit normal vector $\hat{n}$. Let $\hat{t}_1$ and $\hat{t}_2$ be two independent tangent vectors in the sheet and imagine the mean concentration gradient in the plane of the sample to be in $\hat{x}$ then,

$$\begin{aligned} D_{\text{eff}} &= (\langle(\hat{x}\cdot\hat{t}_1)^2\rangle + \langle(\hat{x}\cdot\hat{t}_2)^2\rangle)D_0 = (1 - \langle(\hat{x}\cdot\hat{n})^2\rangle)D_0 \\ &= (1(d=2), 2/3(d=3))D_0 \end{aligned} \tag{10}$$

The first equality is just the analogue of Eq. 9 applied to the two independent directions in the sheet. Thus, if $\hat{x}$ is contained in the sheet where the fluorophore resides, there is no reduction in D_0, whereas if the normal to the sheet is isotropically distributed, there is a reduction by 2/3.

Eqs. 9 and 10 also illustrate a limitation of our model. If the cell were completely flat, and the ER of uniform composition but composed of cisternae in the center and a random grid of tubes in the limb, then D_{eff} would vary by 2. Only if we averaged over regions large enough to contain a fixed ratio of sheets to tubes would our current formulation hold.

NUMERICAL IMPLEMENTATION

Algorithms

The basic data set consists of a prebleach image and a series of postbleach images, which ideally continue long enough so that the last image is nearly proportional to the prebleach one (assuming no immobile fraction). The code defines $\bar{\rho}$ to be the prebleach image and initializes the density, $\rho(r, 0)$, with the first postbleach image. The subsequent images are then compared with the simulation results as a function of time to fit D_{eff}.

The data are defined with 1- to 2-byte accuracy on a rectangular mesh of points. Centered differences are then used to approximate Eq. 5 in such a way that the conservation of ρ over the entire image is exact. For simplicity in one dimension, define the mesh points as $i = 1, 2, ..N$. Then the current Eq. 1 is defined on half-integer mesh points as

$$j_{i+1/2} = 0.5(\bar{\rho}_{i+1} + \bar{\rho}_i)((\rho/\bar{\rho})_{i+1} - (\rho/\bar{\rho})_i) \tag{11}$$

and at the boundaries $j_{1/2} = j_{N+1/2} = 0$.

Approximate Eq. 5 for a time step δ as (with an analogous term for the divergence of $\vec{j}$ in the other dimension),

$$\rho_i(t + \delta) = \rho_i(t) + \delta(j_{i+1/2} - j_{i-1/2}) \quad (12)$$

For any δ, $\Sigma_i\rho_i$ is the same for all times. Numerical stability limits δ to 1/4 in two dimensions, and we have found it more than accurate enough when following photobleach recovery to use $\delta = 1/8$ and stay with this very primitive first order explicit in time algorithm, rather than attempt something higher order or implicit (Press et al., 1992). The simulation code is available from the first author.

Data and efficiency issues

The real experimental images have a nonzero background intensity from regions where there are no cells, and pixel to pixel fluctuations due to noise in the electronics. Occasionally there will be saturation, which if extensive, makes the image unusable for quantitative purposes.

Before subtracting the background, we smooth the data to eliminate the pixel-pixel fluctuations. This is most easily done by iterating the transformation,

$$\rho'_{i,j} = \rho_{i,j} + \delta(\rho_{i+1,j} + \rho_{i-1,j} + \rho_{i,j+1} + \rho_{i,j-1} - 4\rho_{i,j}), \quad (13)$$

which is simply the diffusion equation on the data grid. This is repeated until the pixel-to-pixel variation falls to a preset level. In practice we always work with cells that span at least 100 pixels, bleach regions of at least 20 to 30 pixels, and only fit to experiment intensities averaged over at least 10×10 pixel blocks, so this initial smoothing does not materially alter the data. A histogram of the density is then made for all points in the image, and the most common intensity value is defined as the background. The optimal smoothing and background are determined from the prebleach data and used on all subsequent images in the series.

The background is then subtracted from all points, and negative values are reset to 0 in all the postbleach images. Negative values in the prebleach image are reset to a small positive value of 0.5 (on a scale of 0–255 for 1 byte data), since $\bar{\rho}$ occurs in the denominator of Eq. 5. (The actual value is immaterial, provided it is small.) The total intensity added to $\bar{\rho}$ is 0.17% of the total for the data used in this paper.

The simulation is run until the final density is within a few units (on a 255 scale) of its asymptotic value, as measured by the norm ($\langle\ \rangle$ denotes spatial average),

$$N = \left\langle \bar{\rho} \left| \rho(r, t) - \bar{\rho}(r) \frac{\langle\rho\rangle}{\langle\bar{\rho}\rangle} \right| \right\rangle \Big/ \langle\bar{\rho}\rangle \quad (14)$$

To fit the effective diffusion constant, the user selects one or more boxes on the prebleach image, the time series of experimental images are smoothed and background subtracted and the intensity averaged over the selected box(es). The intensities are now on the same scale as the numerical simulation, and it remains only to translate from the space-time units of the numerical simulation to physical ones, in order to determine D_{eff}.

The time to converge the diffusion equation by an explicit time stepping scheme scales as the fourth power of the mesh size (versus mesh squared for a good implicit scheme; Press et al., 1992). However most of the time is spent removing the variation on the large scales. Thus for the modest accuracy requirements necessary for biological imaging, one can just coarsen the mesh after the highest wavenumbers have relaxed. In practice we integrate for a time large enough for a line 1 pixel wide to spread to 4 pixels and I in Eq. 7 to decrease by 4. Pairs of pixels are then averaged in both x and y to cut the mesh size by 2. If this operation is repeated twice, then on a modern work station a 512^2 image requires a few minutes to run to completion.

Two variants of the standard photobleach recovery experiment can easily be handled with our code. In a fluorescence loss in photobleaching (FLIP; Cole et al., 1996) experiment, a fixed region of the cell is repeatedly bleached, and the fluorescence elsewhere in the cell is monitored. If all material is mobile and in a connected compartment, then ultimately all fluorescence will disappear. To simulate this, we initialize $\bar{\rho}$ with the prebleach image set $\rho = \bar{\rho}$, and at every time step zero ρ within the bleach box. The data processing and fit of D_{eff} are done as before.

It is sometimes convenient to bleach a strip across the cell and then image only that strip during the recovery. Instrumental considerations often dictate this protocol for rapidly diffusing species, in which case significant diffusion has already occurred at the time of the first postbleach image. If the bleach reduces the strip intensity to zero, then the simulation is easy: merely initialize to the prebleach image, numerically zero the strip, and follow the simulation forward. If the bleach reduces the initial intensity in the strip to a fraction γ_p of its initial value, then schematically one should subtract $\gamma_p\bar{\rho}$ from the entire image as in Eq. 6, then zero the strip region, simulate and add back $\gamma_p\bar{\rho}$ at each time point to get the value to be compared with experiment. In practice γ_p is not known, so it has to be fit along with the time scale to the experiment, i.e.,

$$\int_{\text{strip}} dr\rho_{\text{exp}}(r, t) = (1 - \gamma_i)(1 - \gamma_p)\int_{\text{strip}} dr\rho(r, \lambda t) + \gamma_p\int_{\text{strip}} dr\bar{\rho}(r) \quad (15)$$

where we have also allowed for an immobile fraction γ_i, and the experimental densities are background subtracted. The solution of Eq. 5, which appears on the right hand side of Eq. 15, satisfies $\rho(r, 0) = 0$ and $\rho(r, \infty) = \bar{\rho}(r)$ and λ is the temporal scale factor which determines D_{eff}. It has been assumed that the bleach removes a negligible fraction of the

total cell fluorescence. Since these strips are ≥ 2 μm wide, diffraction effects can be adequately accounted for by defining w to be the width measured at half the maximum intensity.

RESULTS

We now fit an experiment in which the ER of a mammalian culture cell was labeled with a galactosyltransferase tagged with GFP; a fraction of the cell was bleached, and the recovery monitored over time (Sciaky et al., 1997). Both the bleaching and imaging were done on a Zeiss 410 confocal microscope which generated rather noisy 1 byte per pixel image files (intensity range, 0–255). To ensure that the fusion protein was retained in the ER throughout the experiment, cells were incubated with the drug brefeldin A, which blocks protein egress from the ER. This type of data is a good test of the robustness of our algorithms, and the errors made in the various steps of data reduction and simulation are presented below.

Fig. 2 shows the experimental prebleach, first postbleach, and final images. The code reports on the percentage of saturated pixel values in all the images that were analyzed, which for the first two images mentioned, amounts to 0.1% and 0.06%, respectively. The code then smooths the prebleach image, which in this case required 26 iterations of Eq. 13 on the whole 512^2 image to reduce the average root mean square variation between each pixel and its 4 neighbors to the target of 2.5. This transformation will spread the intensity on a single pixel to a Gaussian spot of radius 3.5. Fig. 3 shows a histogram of pixel intensity values before and after smoothing. The peak at 1 in Fig. 3 *a* comes from the large dark areas away from the cell, and the single pixel speckle throughout the images gives the spike around 60. After smoothing, the maximum in the distribution moves to 4, which becomes the background value to subtract, the peak at 60 disappears, and there are no pixels with intensity over 230. The integrated intensity from 0 to 7 of the two histograms is unchanged.

How these various manipulations will impact the diffusion constant fit can be quantified by monitoring the intensity changes averaged over the 10×10 supergrid we use in comparing theory and experiment, Table 1. The average errors of smoothing are of the order of 1%, and the largest percentage error occurs in the lowest intensity box, and thus represents an error of only 1% with respect to the mean box intensity. Our automated technique of determining the background intensity could fail if the cell occupied most of the image, so the user can override the internal value. The final processing step resets all negative pixels to 0.5 and 0.0 in the prebleach and all postbleach images, respectively. The averaged intensities change by less than 0.5% and the actual numbers for the first post bleach image are given in Table 1.

The final step in processing the experimental images is to select a rectangular region of interest (ROI) that contains the cell being studied (or enough of it to account for the diffusive recovery). We did not zero out the second cell above the one that was bleached in Fig. 2 *b*, since it is far enough from the bleached region, and there is enough of a gap

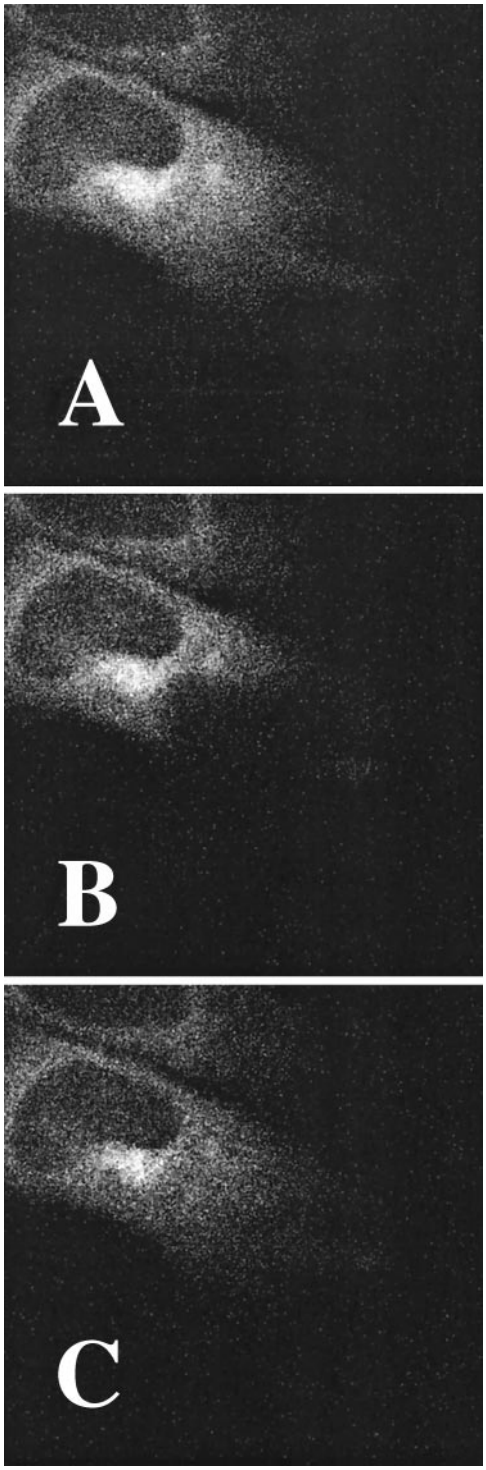

FIGURE 2 Three confocal 512^2 images showing photobleaching and recovery of GFP-galactosyltransferase in the ER. (*a*) Prebleach image. (*b*) First postbleach image. (*c*) Final image (i.e., after recovery).

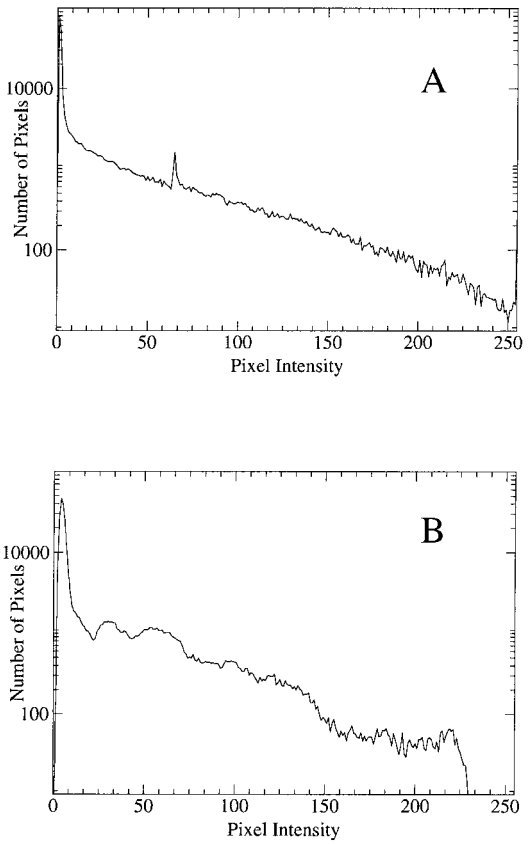

FIGURE 3 Histogram of number of pixels versus intensity for the full 512^2 prebleach image (*a*) before smoothing and (*b*) after smoothing.

between the two cells to minimize the spurious flow of material inputed by the code. The result of all these preprocessing steps is shown in Fig. 4, which are the prebleach, first postbleach (with 10×10 grid), and simulated final postbleach images, respectively. These are the inputs and output of the simulation where panel (a) is $\bar{\rho}$, panel (b) is the initial ρ and (c) is the final ρ. After the remaining experimental postbleach images are similarly processed, we begin the simulation. The two norms that characterize small scales, I Eq. 7, and large scales, N Eq. 14, are 0.15 and 25.8, respectively, for the first postbleach image. The program coarsens the image after 32 and 160 time steps when $I =$ 0.011, $N = 25.5$ and $I = 0.003$, $N = 24.8$ respectively. The program took 94752 times steps to reach the target of $N = 1$, at which time I had decreased to the altogether negligible value of $\sim 10^{-6}$. If the coarsening steps are omitted, and the initial grid used throughout the simulation the typical errors

TABLE 1 The errors due to various data transformations involved in simulating the photobleach experiment in Fig. 2

Process	Average Deviation	Maximum Deviation
Smoothing	1.2%	6.8%
Zeroing pixels	~0.4%	NA
Coarsening	0.25%	3.2%

The first two operations are applied to the experimental data as explained in the text, and the third refers to the computational mesh used in the simulation.

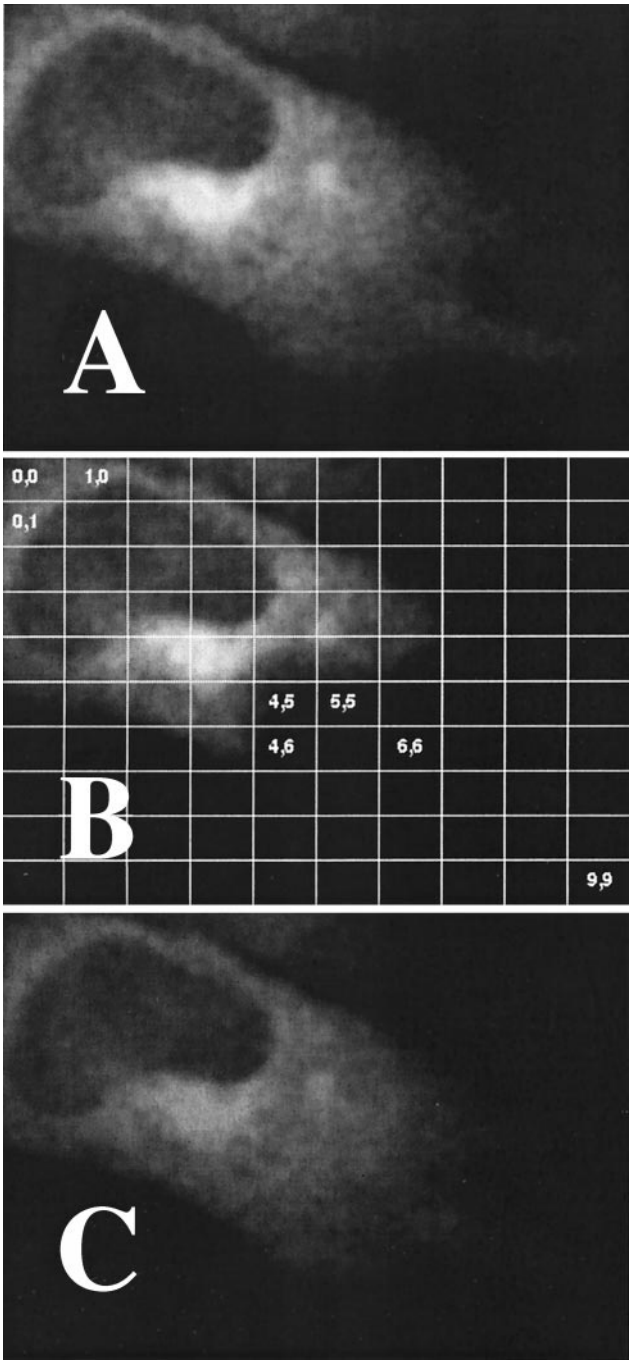

FIGURE 4 The smoothed and background subtracted region of interest used to model the photobleach in Fig. 2. Part (a) is the prebleach image $\bar{\rho}(x)$, (i.e., Fig. 2 *a*); (b) the first postbleach image $\rho(r, 0)$, (i.e., Fig. 2 *b*) with the numbered grid boxes for averaging the intensity; and (c) the final simulated intensity $\rho(r, \infty)$.

in box averaged intensities are less than 1%, Table 1, except in regions of low absolute intensity: 95,143 steps were required to terminate the integration at $N = 1$, very close to the value with coarsening.

Once the user has input the physical pixel size (0.125 μm in our example) and the physical times at which the recovery was monitored, a value of D_{eff} could be determined for each box in Fig. 4 *b*. In Fig. 5, we show a sampling of boxes in the bleached region, which recover at ostensibly different initial rates, yet are all fit by nearly the same D_{eff}. Note that the experiments were terminated well before complete recovery but are consistent with there being no immobile fraction within the scatter for the experimental time course. We illustrate this by rescaling the simulation in boxes (4,6) and (6,6) with a $D_{\text{eff}} = 0.5$ and 15% immobile fraction (thin solid line in Fig. 5). Although the fits appear to be slightly better than those with $\gamma_i = 0$, they can be rather ambiguous when the experiments have not run to long enough times for a clear asymptotic plateau to be visible. Random errors in the data translate into about a 20% uncertainty in D_{eff} as shown by the two bracketing curves for the second data set. The same diffusion constant should apply to the regions whose fluorescence decreases during recovery, a sampling of which is shown in Fig. 6. The scatter is somewhat larger than before, perhaps because the percentage change in intensity is much less. Some of the variation may be due to the change in effective dimensionality of the ER between the center and periphery of the cell, which can change D_{eff} by a factor of 1.5 (cf. Eqs. 9 and 10). Note also that the fourth curve in Fig. 6 does not approach its asymptote monotonically. The fluorescence hits a minimum because of the many channels connecting box (4,3) with the bleached region. The slow increase from the minimum results from weak connections with more remote regions of the cell. The computational grid coarsening did not affect the fits of D_{eff} to the precision shown.

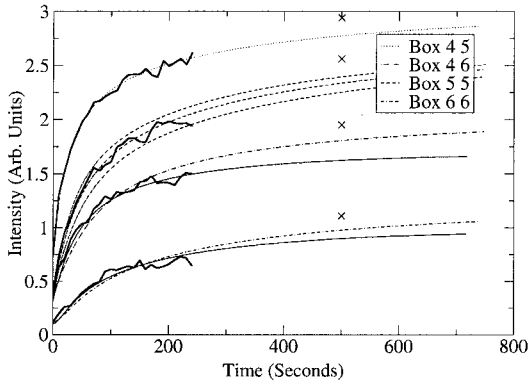

FIGURE 5 Plots of the experimental recovery (*heavy solid lines*) and the simulation for several of the grid boxes shown in Fig. 4 *b*. With no immobile fraction the fit of D_{eff} gives 0.29, 0.29, 0.30, and 0.34 μm^2/s for boxes (4,5), (4,6), (5,5), and (6,6), respectively. The two dashed curves bracketing the preferred fit for (5,5) show the effect of varying D_{eff} by 20%. The thin solid curves for boxes (4,6) and (6,6) assume an immobile fraction of 15% and give $D_{\text{eff}} = 0.5$. The $\times$ marks the prebleach intensities to which the experiment would recover if there were no immobile fraction.

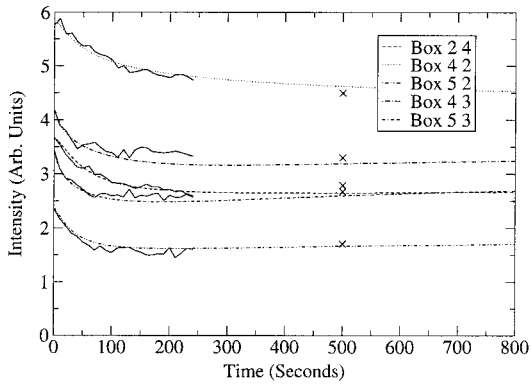

FIGURE 6 Plots of the experimental recovery (*solid lines*) and simulation for several grid boxes labeled as in Fig. 4 *b* where the intensity decreases. The fit with no immobile fraction gives $D_{\text{eff}} = 0.34$, 0.37, 0.40, 0.25, and 0.25 μm^2/s for boxes (2,4), (4,2), (5,2), (4,3), and (5,3), respectively. The crosses denote the simulation intensities at full recovery ($\sim$1200 s in this example).

It is sometimes possible to get a reasonable estimate of D_{eff} by bleaching a strip of width w across a cell and fitting the recovery to the approximate formula

$$I(t) = I(\infty)(1 - (w^2(w^2 + 4\pi D_{\text{eff}}t)^{-1})^{1/2}) \qquad (16)$$

presented in Ellenberg et al. (1997). It is assumed that the bleach is complete, there is no immobile fraction, the cell is a uniform rectangle, the strip is normal to the long direction, and w is much less than the distance to either end. Fig. 7 shows the pre-processed image of a mitotic cell in which a $w = 4$ μm strip was removed numerically. The recovery was then simulated with our code and an assumed diffusion constant of 1 μm^2/s. The fit to Eq. 16 was very good but gave $D_{\text{eff}} = 1.35$, Fig. 8, rather than 1. Similar experiments with the strip centered and near the lower edge gave $D_{\text{eff}} =$ 1.31 and 1.11, respectively. The disparities between Fig. 7 and the idealization necessary for Eq. 16 to apply can push D_{eff} either up or down in comparison with 1. The finite extent of the cell decreases the time necessary to reach the asymptote and increases the D_{eff} implied by Eq. 16; placing the strip at the edge of a strictly rectangular cell, is equivalent to a strip twice as wide in the middle of a cell twice as long, decreasing D_{eff} by 4. The quality of the fit is worse with the strip on the edge, as expected, and the curvature of the cell there largely counteracts the theoretical reduction in D_{eff}.

DISCUSSION

The ability to simulate diffusion in a generally inhomogeneous but isotropic material is the first essential step in modeling diffusion in live cells, but there are many complicating issues for which a general treatment is impossible,

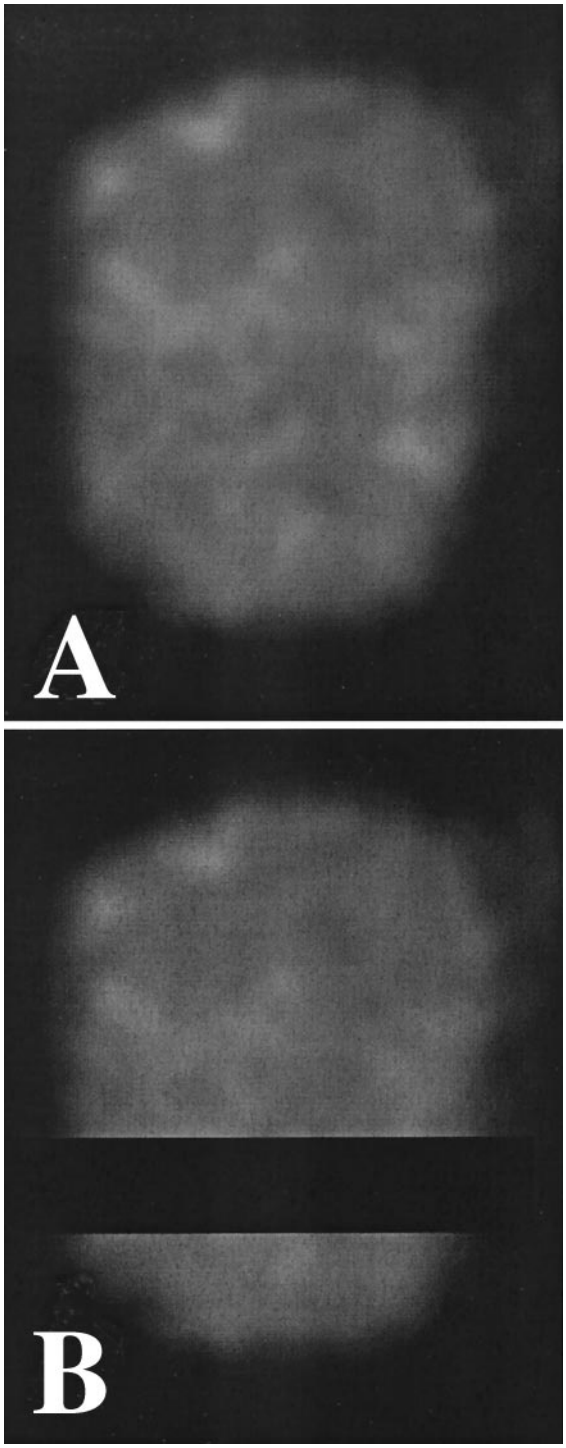

FIGURE 7 Smoothed and background subtracted images of a cell (*A*) before and (*B*) after a 4-μm strip was zeroed across the length of the cell to generate synthetic data to test the 1D diffusive recovery formula shown in Eq. 16.

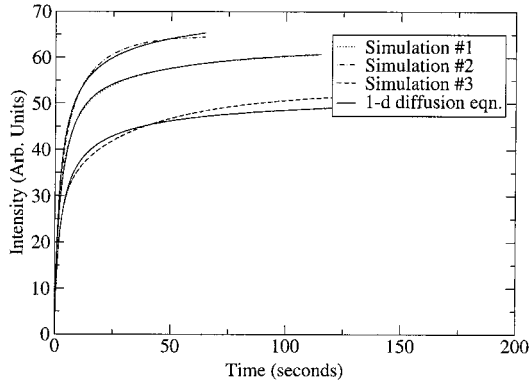

FIGURE 8 Comparison of a fit of Eq. 16 to the results of the simulation (solid curve) for the data in Fig. 7 *a*. Simulation 1 is recovery into the 4-μm bleach strip in Fig. 7 *b*; simulation 2, the same strip moved 5.2 μm higher; and simulation 3, the same strip moved 3.2 μm lower than Fig. 7 *b*. The fit of Eq. 16 gives $D_{\text{eff}} = 1.35$, 1.31, and 1.11 for these three cases, versus a value of 1.0 used in the simulation of the full cell image, which defines the data.

and one must deploy biophysical methods in a way that optimizes the prospects for quantitative analysis. For this purpose we provide some intuitive guides grouped loosely around complexities of geometry, other dynamical processes, and immobile fractions.

Both our experiments and analysis have dealt with cells viewed in projection. Our model as embodied in Eq. 5 readily generalizes to three dimensions. If it applies to the ER in real cells, then it is a mathematical consequence that neglect of the third dimension is inconsequential, provided the scale of variation in the lateral dimensions is large compared with the thickness. However, it is anticipated that a variation of 50% can occur in D_{eff} (cf. Eqs. 9 and 10) as one proceeds from a region where the orientation of the tubes and cisternae are random in a volume to one where they are random only in the plane. The variation in D_{eff} can be as large as a factor of 3 if the ER is entirely tubular, randomly oriented in one region, entirely aligned in an adjacent one, and the bleach box is normal to the aligned tubes (i.e., diffusion follows D_0 in the latter region). The fundamental assumption embodied in Eq. 5 is that the density of fluorescence represents equally well the density of connections, i.e., the flux is proportional to $\bar{\rho}$, Eq. 1. The measured intensity has to be averaged over a spacial region larger than the interconnection scale e.g., a few microns (Terasaki et al., 1986). Our model completely fails when two compartments which overlap in projection are actually disconnected in 3D.

The pathways by which the cell targets newly synthesized proteins and internalizes material from the outside involve a series of disconnected membrane-bound organelles. The physical separation between organelles is essential since they have different lipid and protein components, but it requires elaborate mechanisms to separate substrate from the organelle resident enzymes and target it to the next compartment. The Golgi complex receives secretory cargo exported from the ER and appears at the optical level as

multiple compact structures, some of which are disconnected, as shown by photobleach (Cole et al., 1996). To determine the diffusive mobility within the Golgi complex requires care since structures which appear continuous in projection are actually disconnected. The strategy adapted by Cole et al. (1996) was to bleach a narrow strip across a single structure and ideally remove only a small fraction of the structure's total fluorescence. An alternative strategy is to bleach one of two structures ostensibly connected by a narrow neck in a projected image. If recovery is very slow, they are not connected. Otherwise, the situation resembles that in Fig. 1, and if the density in the neck can be measured D_{eff} can be inferred.

We have found that many images of GFP chimeras in the ER can show bright spots on a diffuse background. If the entire region is bleached and the material in the spot is both connected to the rest of the fluorescence pool and not subject to any special localization, then the recovery of the entire image would be described by our simulation. If the spot does not recover, then it was probably disconnected from the ER, whereas if the recovery is faster than diffusive, some process is actively concentrating material.

The most general point to be made is that the ability to simulate the entire cell liberates the experimenter from bleaching the smallest region possible in order to fit to the usual formulas for a homogeneous media. Thus, one should exercise the freedom to bleach a variety of shape and size patterns, in different locations in the cell and verify that one D_{eff} fits all. One should also compare a FLIP experiment in which the entire cell is drained of fluorescence by repeatedly bleaching one region, with the more conventional fluorescence recovery after photobleaching (FRAP). If the same D_{eff} fits both, it is a stringent test that all material is in a single connected compartment with evidently very homogeneous properties throughout. Finally, because recovery usually is very gradual into the limb of the cell (cf. box 6,6 in Fig. 5), the experiment should be run long enough to reliably estimate if there is an immobile fraction. As shown in Fig. 5, we can achieve slightly better fits by adding γ_i as a fitting parameter. However this additional degree of freedom allows one to fit partially recovered or even cropped data as though it is fully recovered, and thereby arrive at meaningless values for D_{eff} and γ_i.

The ability to bleach a defined region is particularly important when some fraction of the image is immobile or subject to different dynamics. In the simplest case, the immobile component is a fixed fraction of the total, and after some rescalings that we have outlined, the quality of the fits between simulation and experiment should be no worse than in the ideal case when everything is mobile. But imagine one is viewing the plasma membrane (PM) for a marker also present in the Golgi complex and thus disconnected from the time scale of the experiment. One strategy at the computer processing level would be to excise the Golgi complex from the prebleach image (and perhaps fill in with the PM intensity in the neighborhood) and only then run the simulation. Alternatively, in the experiment, one could photobleach the Golgi, allow the fluorescence to recover in the PM that was also bleached and then do a second bleach on the PM and compare with the standard simulation. (The first recovery must be run to completion only to determine $\bar{\rho}$. If an alternate means can be found to determine the steady-state density in the PM, such as confocal microscopy, then a single bleach will suffice.) In either case, the bleach that determines D_{eff} should be as far from the irrelevant pool as possible and sufficiently small that the material necessary for recovery comes from nearby.

We have found no general robust and practical method for determining an immobile fraction cell-wide that is not a fixed multiple of $\bar{\rho}(r)$. One way of understanding the practical problems is to decompose the prebleach image, $\rho_0(r)$, and the final image, $\rho_\infty(r)$, into a mobile density $\rho_m(r)$ and an immobile density $\rho_i(r)$,

$$\rho_0(r) = \rho_i(r) + \rho_m(r),\ \rho_\infty(r) = \chi(r)\rho_i(r) + \alpha\rho_m(r) \qquad (17)$$

where $\chi(r) = \gamma_p < 1$ in the bleached region (assumed known) and 1 elsewhere, and $\alpha = \int\chi(r)\rho_m(r)/\int\rho_m(r)$ is the fraction of the mobile pool that was bleached. It is only $\rho_m(r)$ that is time-dependent, and to integrate Eq. 5 requires setting $\bar{\rho} = \rho_m(r)$; i.e., $\rho_m(r)$ must be known. Eq. 17 can be inverted point by point; however, both γ_p and α cannot be simultaneously determined from Eq. 17, since the right-hand sides are not independent at all points, i.e., $\int\chi\rho_0 = \int\rho_\infty$. The parameter γ_p can be found by fitting Eq. 17 to the boundary of the bleached region and assuming both $\rho_{m,i}$ are uniform over the step created by the bleach, but even when γ_p is known, the self-consistent equation for α is not easy to solve.

The real problems in inverting Eq. 17 have to do with time scales and experimental errors. The immobile fraction has to be absolutely immobile for a time long enough for $\rho_m(r)$ to relax over the whole cell. Naturally, one is less sensitive to regions farthest from the bleach box, and vulnerable to large errors if part of the cell moves. As a consequence, if one inverts Eq. 17 formally (for example, by doing the experiment where $\gamma_p \sim 0$), there will be isolated points where $\rho_i(r) < 0$ for values of α near 0 or 1. In practice there frequently remains only a rather small interval of allowed α values. Under typical conditions, where the immobile fraction is merely slow and parts of the cell do move around, it is very hard to automatically determine $\rho_{m,i}$ cell-wide. The best strategy seems to be bleaching an alternating on/off pattern across the entire cell so that the recovery occurs locally and rapidly.

Until now the plasma membrane was the prototypical membrane for biophysical studies of lateral protein mobility (Edidin, 1994). In this system, intrinsic membrane proteins can have diffusion constants in the range of 0.01 to 0.1 $\mu m^2/s$, and some degree of short term localization as man-

ifested by less than complete recovery. There is also a dependence of the ostensible D_{eff} on bleach spot size for scales below 1–2 μm, which has been interpreted in terms of a fast and slow diffusing pool (Edidin, 1994).

By contrast, our measurements probe only scales larger than a few microns. We have found D_{eff} for many GFP-tagged transmembrane proteins in intracellular compartments to be in the range of 0.3 $\mu m^2/s$ with 80–100% recovery (Sciaky et al., 1997; Ellenberg et al., 1997). This implies a microscopic D_0 applicable to a flat membrane of up to $\sim$1 $\mu m^2/s$, comparable to diffusion times in synthetic bilayers. Our measurements of D_{eff} are quantitatively reproducible over many cells and in many subregions within each cell. Other transport mechanisms that might appear like diffusional transport, including movement of detached vesicles, can be ruled out by the conceptually simple but technically difficult biophysical technique of measuring both a protein and lipid diffusion constant (Zaal et al., 1999). If transport were by vesicles, both protein and lipid would recover at the same rate. The consistency of different D_{eff} for Golgi and ER protein and lipids during mitosis (Zaal et al., 1999), and after treatment with brefeldin A provides evidence that vesicle processes for moving Golgi and ER markers are not occurring under these conditions. Viewed on the scale of microns, the ER membrane system is as amenable to study as the plasma membrane, and biophysical methods, if sufficiently quantitative, allow indirect inferences about transport processes in live cells whose study previously required biochemical or genetic manipulations.

S.B. and E.D.S. were supported in part by the National Institutes of Health under grant number GM59018-01. A. Kenworthy and J. Presley provided a critical reading of the manuscript.

REFERENCES

Cole, N. B., C. L. Smith, N. Sciaky, C. L. Smith, M. Terasaki, M. Edidin, and J. Lippincott-Schwartz. 1996. Diffusional mobility of Golgi proteins in membranes of living cells. *Science.* 273:797–801.

Dayel, M. J., E. F. Hom, and A. S. Verkman. 1999. Diffusion of green fluorescent protein in the aqueous-phase lumen of endoplasmic reticulum. *Biophys. J.* 76:2843–2851.

De Giorgi, F., Z. Ahmed, C. Bastianutto, M. Brini, L. S. Jouaville, R. Marsault, M. Murgia, P. Pinton, T. Pozzan, and R. Rizzuto. 1999. Targeting GFP to organelles. *Methods Cell Biol.* 58:75–85.

Edidin, M. 1994. Fluorescence photobleaching and recovery, FPR, in the analysis of membrane structure and dynamics. *In* Mobility and Proximity in Biological Membranes. S. Damjanovich, M. Edidin, J. Szollosi, and L. Tron, Eds. CRC Press, Boca Raton, FL. 109–135.

Edidin, M. 1997. Lipid microdomains in cell surface membranes. *Curr. Opin. Struct. Biol.* 7:528–532.

Ellenberg, J., E. D. Siggia, J. E. Moreira, C. L. Smith, J. F. Presley, H. J. Worman, and J. Lippincott-Schwartz. 1997. Nuclear membrane dynamics and reassembly in living cells: targeting of an inner nuclear membrane protein in interphase and mitosis. *J. Cell Biol.* 138:1193–1206.

Ellenberg, J., J. Lippincott-Schwartz, and J. Presley. 1999. Dual-colour imaging with GFP variants. *Trends Cell Biol.* 9:52–56; and other articles therein.

Hirschberg, K., C. M. Miller, J. Ellenberg, J. F. Presley, E. D. Siggia, R. D. Phair, and J. Lippincott-Schwartz. 1998. Kinetic analysis of secretory protein traffic and characterization of Golgi to plasma membrane transport intermediates in living cells. *J. Cell Biol.* 143:1485–1503.

Kubitscheck, U., P. Wedekind, and R. Peters. 1994. Lateral diffusion measurement at high spatial resolution by scanning microphotolysis in a confocal microscope. *Biophys. J.* 67:948–956.

Lippincott-Schwartz, J., J. F. Presley, K. J. Zaal, K. Hirschberg, C. D. Miller, and J. Ellenberg. 1999. Monitoring the dynamics and mobility of membrane proteins tagged with green fluorescent protein. *Methods Cell Biol.* 58:261–281.

Marguet, D., E. T. Spiliotis, T. Pentcheva, M. Lebowitz, J. Schneck, and M. Edidin. 1999. Lateral diffusion of GFP-tagged H2Ld molecules and of GFP-TAP1 reports on the assembly and retention of these molecules in the endoplasmic reticulum. *Immunity.* 11:231–240.

Nakata, T., S. Terada, and N. Hirokawa. 1998. Visualization of the dynamics of synaptic vesicle and plasma membrane proteins in living axons. *J. Cell Biol.* 140:659–674.

Nehls, S., E. L. Snapp, N. B. Cole, K. J. M. Zaal, A. K. Kenworthy, T. H. Roberts, J. Ellenberg, J. F. Presley, E. Siggia, and J. Lippincott-Schwartz. 2000. Dynamics and retention of misfolded proteins in native ER membranes. *Nat. Cell Biol.* 2:288–295.

Olveczky, B. P., and A. S. Verkman. 1998. Monte Carlo analysis of obstructed diffusion in three dimensions: application to molecular diffusion in organelles. *Biophys. J.* 74:2722–2730.

Peters, R. 1999. Scanning microphotolysis: three-dimensional diffusion measurement and optical single-transporter recording. *Methods.* 18: 508–517.

Polishchuk, R. S., E. V. Polishchuk, P. Marra, S. Alberti, R. Buccione, A. Luini, and A. A. Mironov. 2000. Correlative light-electron microscopy reveals the tubular-saccular ultrastructure of carriers operating between Golgi apparatus and plasma membrane. *J. Cell Biol.* 148:45–58.

Presley, J. F., N. B. Cole, T. A. Schroer, K. Hirschberg, K. J. Zaal, and J. Lippincott-Schwartz. 1997. ER-to-Golgi transport visualized in living cells. *Nature.* 389:81–85.

Press, W., S. A. Teukolsky, W. T. Vetterling, and B. P. Flannery. 1992. Numerical Recipes in C. Cambridge University Press, Cambridge.

Scales, S. J., R. Pepperkok, and T. E. Kreis. 1997. Visualization of ER-to-Golgi transport in living cells reveals a sequential mode of action for COPII and COPI. *Cell.* 90:1137–1148.

Sciaky, N., J. Presley, C. Smith, K. J. Zaal, N. Cole, J. E. Moreira, M. Terasaki, E. Siggia, and J. Lippincott-Schwartz. 1997. Golgi tubule traffic and the effects of brefeldin A visualized in living cells. *J. Cell Biol.* 139:1137–1155.

Subramanian, K., and T. Meyer. 1997. Calcium-induced restructuring of nuclear envelope and endoplasmic reticulum calcium stores. *Cell.* 89: 963–71.

Szczesna-Skorupa, E., C-D. Chen, S. Rogers, and B. Kemper. 1998. Mobility of P450 in the endoplasmic reticulum. *Proc. Natl. Acad. Sci. USA.* 95:14793–14798.

Terasaki, M., L. B. Chen, and K. Fujiwara. 1986. Microtubules and the endoplasmic reticulum are highly interdependent structures. *J. Cell Biol.* 103:1557–1568.

Terasaki, M., L. A. Jaffe, G. R. Hunnicutt, and J. A. Hammer 3rd. 1996. Structural change of the endoplasmic reticulum during fertilization: evidence for loss of membrane continuity using the green fluorescent protein. *Dev. Biol.* 179:320–328.

Toomre, D., P. Keller, J. White, J.-C. Olivo, and K. Simons. 1999. Dual-color visualization of trans-Golgi network to plasma membrane traffic along microtubules in living cells. *J. Cell Sci.* 112:21–33.

Tsien, R. Y. 1998. The green fluorescent protein. *Annu. Rev. Biochem.* 67:509–544.

Wang, M. C., and G. E. Uhlenbeck. 1945. On the theory of Brownian motion. *Rev. Mod. Phys.* 17:323–342.

Zaal, K. J., C. L. Smith, R. S. Polishchuk, N. Altan, N. B. Cole, J. Ellenberg, K. Hirschberg, J. F. Presley, T. H. Roberts, E. Siggia, R. D. Phair, and J. Lippincott-Schwartz. 1999. Golgi membranes are absorbed into and reemerge from the ER during mitotis. *Cell.* 99:589–601.